Journal of Computational Physics 256 (2014) 118–134

Contents lists available at ScienceDirect

Journal of Computational Physics

www.elsevier.com/locate/jcp

A conservative multi-tracer transport scheme for spectral-element spherical grids

Christoph Erath [a,*], Ramachandran D. Nair [b]

[a] University of Vienna, Faculty of Mathematics, Oskar-Morgenstern-Platz 1, 1090 Vienna, Austria
[b] National Center for Atmospheric Research, [1] 1850 Table Mesa Drive, Boulder, CO 80305, USA

ARTICLE INFO

Article history:
Received 1 May 2013
Received in revised form 14 August 2013
Accepted 19 August 2013
Available online 3 September 2013

Keywords:
Conservative semi-Lagrangian
Multi-tracer transport
Cubed sphere
Spectral-element grid
Multi-moment reconstruction
Flux-corrected transport
Characteristic semi-Lagrangian
Parallelization
Scalability

ABSTRACT

Atmospheric models used for practical climate simulation must be capable handling the transport of hundreds of tracers. For computational efficiency conservative multi-tracer semi-Lagrangian type transport schemes are appropriate. Global models based on high-order Galerkin approach employ highly non-uniform spectral-element grids, and semi-Lagrangian transport is a challenge on those grids. A conservative semi-Lagrangian scheme (SPELT — SPectral-Element Lagrangian Transport) employing a multi-moment compact reconstruction procedure is developed for non-uniform quadrilateral grids. The scheme is based on a characteristic semi-Lagrangian method that avoids complex and expensive upstream area computations. The SPELT scheme has been implemented in the High-Order Method Modeling Environment (HOMME), which is based on a cubed-sphere grid with spectral-element spatial discretization. Additionally, we show the (strong) scalability and multi-tracer efficiency using several benchmark tests. The SPELT solution can be made monotonic (positivity preserving) by combining the flux-corrected transport algorithm, which is demonstrated on a uniform resolution grid. In particular, SPELT can be efficiently used for non-uniform grids and provides accurate and stable results for high-resolution meshes.

1. Introduction

In the past two decades, global spectral methods have dominated in atmospheric modeling. However, the main disadvantage of these methods is that they require expensive non-local communication operations, which prevents them from using the full potential of available massive parallel petascale computers. In recent years, high-order accuracy is being achieved by using finite-element type models, including the spectral-element (SE) or continuous Galerkin and the discontinuous Galerkin (DG) methods (see [31,32,14,26]). These element-based and high-order Galerkin methods have the nice feature that the data for parallel communication is reduced to a minimum due to localized computations. Additionally, element-based methods allow a more flexible choice of domain and local mesh refinement as, for example, spectral methods.

The spectral-element dynamical core [31] based on the High-Order Method Modeling Environment (HOMME) [8] framework is the default dynamical core for the Community Atmosphere Model (CAM, version 5.2 and higher) — CAM-SE. The grid system in HOMME is based on the cubed-sphere geometry resulting from a gnomonic equiangular projection of the sphere. It has been shown in [7] that this approach is highly scalable, up to 170 000 cores on the Oak Ridge LCF Cray XT5 JaguarPF system. However, with a growing number of tracers in today's atmospheric modeling applications transport becomes a

* Corresponding author.
E-mail addresses: christoph.erath@univie.ac.at (C. Erath), rnair@ucar.edu (R.D. Nair).

[1] The National Center for Atmospheric Research is sponsored by the National Science Foundation.

0021-9991/$ – see front matter
http://dx.doi.org/10.1016/j.jcp.2013.08.050

dominating factor of the total computational costs; for example, more than $O(100)$ tracers are used in the current chemistry version of CAM, and this number is likely to increase in future applications. A native SE transport scheme combined with non-oscillatory features is available in HOMME [15]. Unfortunately, it is computationally prohibitive for a large number of tracers due to three communications per time step and a relatively small time step of the explicit Runge–Kutta based approach [7]. In addition, SE advection is coupled with a hyper-diffusion operator that also increases the computational cost.

Thus the multi-tracer transport is a major computational bottleneck of the HOMME dynamical core for climate simulations. Furthermore, HOMME supports unstructured grids. Therefore it is desirable to have multi-tracer efficient schemes capable of handling such grid system. Conservative semi-Lagrangian methods with moderate Courant numbers can be employed for efficiently handling the multi-tracer problems [11]. Using a moderate Courant number for the semi-Lagrangian advection does not adversely affect the parallel efficiency of the Eulerian host model. But this Courant number can still be chosen several times larger than that for a high-order advection scheme. Recently, a third-order Conservative Semi-LAgrangian Multi-tracer transport scheme (CSLAM [20]) has been integrated in HOMME [11]. This is achieved by overlaying the HOMME SE grids with uniform finite-volume cells. However, the CSLAM scheme is designed for uniform grids and requires a 5×5 reconstruction stencil (as implemented in HOMME), for which extra interpolations are required at the cube corner (ghost cells). In addition, CSLAM relies on computing the upstream (Lagrangian) areas through an intricate process. For that an expensive search algorithm is needed to locate and compute the overlap areas [20]. This implies that for an arbitrary unstructured cubed-sphere grid, implementation of a finite-volume semi-Lagrangian scheme such as CSLAM may be prohibitively complicated.

In order to preserve the parallel efficiency of the host model HOMME, the multi-tracer transport algorithm should depend only on a compact computational stencil and should also be suitable for unstructured grid systems. The multi-moment based finite-volume approach introduced in [34,3] employs a single-cell reconstruction procedure and is well-suited for our application. The upstream overlap-area computation required for the conservative semi-Lagrangian scheme can be avoided by using the characteristic semi-Lagrangian approach, where the fluxes are integrated along the characteristics as shown in [4]. We further extend this approach for arbitrary quadrilateral grids on the cubed sphere by designing a conservative semi-Lagrangian scheme on the spectral-element grid, hereinafter referred to as SPELT — SPectral-Element Lagrangian Transport. For the SPELT scheme the upstream search is reduced to a point search on the cubed sphere and the reconstruction is local, which makes SPELT extremely attractive for arbitrary grids. SPELT is a conservative flux-based scheme (with a monotonic option) and is accurate on arbitrary quadrilateral grids. Moreover, a new algorithm in HOMME shows that SPELT is highly scalable *and* multi-tracer efficient. The performance of SPELT in climate simulations is beyond the scope of this manuscript and will be discussed in a future work [13].

The remainder of the paper is organized as follows: in Section 2 we briefly describe semi-Lagrangian schemes for the transport equation. Section 3 describes our SPELT algorithm, in particular the scheme for arbitrary quadrilateral grids. Section 4 shows the multi-tracer efficiency, scalability and some high-resolution experiments comparing the relative merits of both schemes in HOMME.

2. Tracer transport schemes

The flux-form transport equation for a scalar $\rho(x, y, t)$ in 2D Cartesian (x, y)-plane, without a source or sink, can be written as follows:

$$\frac{\partial \rho}{\partial t} + \frac{\partial (u\rho)}{\partial x} + \frac{\partial (v\rho)}{\partial y} \equiv \frac{\partial \rho}{\partial t} + \nabla \cdot \mathbf{F} = 0, \quad t \in (0, T], \tag{1}$$

where (u, v) is the wind velocity vector, $\mathbf{F} = (\rho u, \rho v)$ is the flux, and the initial condition is prescribed as $\rho(x, y, t = 0) = \rho_0(x, y)$. Equivalently, (1) can be cast in the following Lagrangian form:

$$\frac{D}{Dt} \int_{\mathcal{A}(t)} \rho \, d\mathcal{A} = 0, \tag{2}$$

where $D/Dt = \partial_t + u\partial_x + v\partial_y$ is the Lagrangian (material) derivative, $\mathcal{A}$ is the area (volume) in which the fluid density ρ evolves in time along the Lagrangian trajectories (characteristics). However for the non-divergent flow fields, a regular semi-Lagrangian approach, which is not constrained to be conservative, uses the following simple form:

$$\frac{D\rho}{Dt} = 0, \quad \Rightarrow \quad \rho^{n+1} = \left[\rho^n\right]^*, \tag{3}$$

where the second equation indicates a semi-Lagrangian time discretization. Here, ρ^{n+1} is the estimate of ρ at the new time level t^{n+1} from known values ρ^n at time $t^n = n\Delta t$. Usually ρ^{n+1} is computed by an interpolation at the foot of the trajectory (upstream position), in (3) this is denoted as $[\cdot]^*$.

Both forms, (1) and (2), are used for numerical discretization of a conservative transport based on Eulerian and Lagrangian methods, respectively. Conservative finite-volume semi-Lagrangian methods such as the cell-integrated semi-Lagrangian schemes (CISL [25], CSLAM [20]) and other schemes based on incremental remapping [9] employ the Lagrangian form (2). These schemes utilize backward trajectories. The upstream or Lagrangian cell corresponding to the arrival cell (or

Eulerian cell, usually a rectangular region) is an arbitrary quadrilateral and overlaps usually more than one regular Eulerian grid cell. The sub-grid scale density distribution in each Eulerian grid cell is often approximated by a polynomial of specific order such that the cell average ($\overline{\rho}$) evolves in time. In order to update the average density at a new time level ($\overline{\rho}^{n+1}$) in the discrete approximation of (2), the mass (area) of the Lagrangian cell needs to be integrated from the underlying Eulerian cells. For *exact* mass conservation (up to machine precision), exact volumes of upstream cell intersections are required and then integrals are calculated over the intersecting volumes [9,17,12]. Although these schemes are robust on structured grids, computation of the mass enclosed in the Lagrangian cells is an expensive and subtle procedure, and is not obvious for non-uniform or arbitrarily unstructured grid systems.

However, by employing the method of characteristics [22], the explicit computation of integrals over upstream Lagrangian cells can be avoided. The fluxes are integrated along the characteristic joining the Eulerian and Lagrangian points, and do not depend on the arbitrary geometrical shape of the Lagrangian cells. Variants of flux-based semi-Lagrangian schemes exploiting ideas of methods of characteristics have been in use for meteorological modeling for a long time [21,23]. Recently, a non-hydrostatic model based on the "flux-based characteristic method" has been developed in [27]. Although there are various names used for different formulations of method of characteristics such as flux-form (or flux-based) semi-Lagrangian method, we prefer to use the name characteristic semi-Lagrangian in the present work. For simplicity, these schemes were developed in a dimension-splitting manner, where the time-integrated fluxes are evaluated at the Eulerian cell walls along each coordinate direction.

We consider the multi-moment semi-Lagrangian scheme developed in [4], where the reconstruction is on a single Eulerian cell and the reconstruction function is a biquadratic polynomial (fully 2D) leading to third-order accuracy. A novel feature of this scheme is that the reconstruction is local to the cell, avoiding the use of a wider halo region. Moreover, the fluxes are evaluated along the characteristics w.r.t. time and therefore there is no need to compute explicit integrals over the upstream Lagrangian cells. We further extend the scheme for non-uniform quadrilateral grids with positivity preservation option and show how the scheme can be made monotonic with a flux-corrected transport approach. Our ultimate goal is to extend the scheme further for the application of transport on unstructured spectral-element grids in HOMME. The resulting scheme, hereinafter referred to as the Spectral-Element Lagrangian Transport (SPELT) scheme, will be described in the next section. The acronym SPELT implies a general approach where the reconstruction could be based on a regular finite-volume or a high-order method. Nevertheless, in the present work this term specifically refers to a transport scheme which relies on a third-order multi-moment reconstruction procedure combined with a characteristic semi-Lagrangian approach. A major motivation for us to adopt multi-moment approach is because of its compact computational stencil which can be packed into spectral-element grids. The SPELT scheme is flexible and may be extended to arbitrary unstructured grids.

3. SPELT — SPectral-Element Lagrangian Transport

This section focuses on the design of our SPELT algorithm on non-uniform quadrilateral grids.

3.1. SPELT reconstructions

The 2D physical domain consists of a non-uniform rectangular grid. The grid cells are convex quadrilaterals C_{kl} such that each cell is mapped onto a unit square with local coordinates $\alpha, \beta \in [0, 1]$. The local mapping from (x, y) physical space to the computational space is given by the following bilinear map:

$$x = a_1 + a_2\alpha + a_3\beta + a_4\alpha\beta, \tag{4}$$

$$y = b_1 + b_2\alpha + b_3\beta + b_4\alpha\beta. \tag{5}$$

Let us denote the Cartesian coordinates for the vertices of the quadrilateral $ABCD$ in Fig. 1 by (x_m, y_m), $m = 1, 2, 3, 4$. Then the coefficients a_m and b_m in (4) and (5) are uniquely determined by

$$\begin{bmatrix} a_1 \\ a_2 \\ a_3 \\ a_4 \end{bmatrix} = \mathbf{M}^{-1} \begin{bmatrix} x_1 \\ x_2 \\ x_3 \\ x_4 \end{bmatrix}, \qquad \begin{bmatrix} b_1 \\ b_2 \\ b_3 \\ b_4 \end{bmatrix} = \mathbf{M}^{-1} \begin{bmatrix} y_1 \\ y_2 \\ y_3 \\ y_4 \end{bmatrix}, \qquad \mathbf{M} = \begin{bmatrix} 1 & 0 & 0 & 0 \\ 1 & 1 & 0 & 0 \\ 1 & 1 & 1 & 1 \\ 1 & 0 & 1 & 0 \end{bmatrix}. \tag{6}$$

The Jacobian of the transformation and the associated metric term are formally defined by

$$\mathbf{J} = \begin{bmatrix} \partial x/\partial\alpha & \partial x/\partial\beta \\ \partial y/\partial\alpha & \partial y/\partial\beta \end{bmatrix}, \qquad \left|\mathbf{J}(\alpha, \beta)\right| = \frac{\partial x}{\partial\alpha}\frac{\partial y}{\partial\beta} - \frac{\partial x}{\partial\beta}\frac{\partial y}{\partial\alpha}. \tag{7}$$

The average value of $\rho(x, y, t)$ over the quadrilateral cell C_{kl} can be defined by

$$\overline{\rho}_{kl}(t) = \frac{1}{|C_{kl}|}\int_{C_{kl}} \rho(x, y, t)\, dx\, dy = \frac{1}{|C_{kl}|}\int_0^1\int_0^1 \rho(\alpha, \beta, t)|\mathbf{J}_{kl}|\, d\alpha\, d\beta, \tag{8}$$

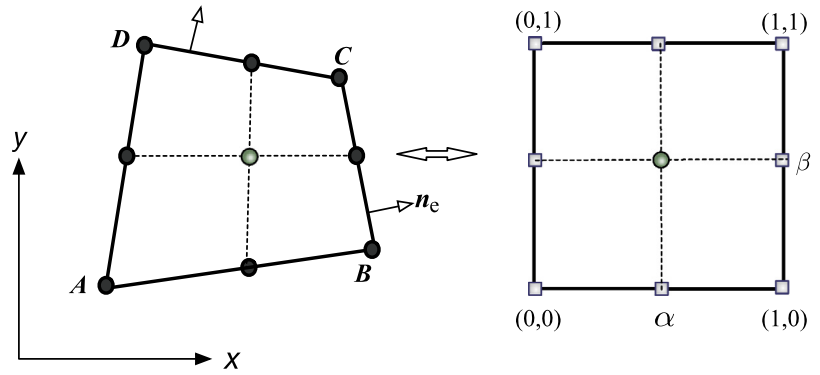

Fig. 1. Schematic diagram showing an arbitrary quadrilateral on the left ($ABCD$) which is mapped onto a unit square $[0,1]^2$ with local coordinates (α,β), as shown on the right panel. Here, $\mathbf{n}_e$ is the unit normal vector pointing outward on the east edge. The multi-moment polynomial reconstruction requires nine degrees of freedom on each cell, which evolve in time. They include eight point values at the corners and edges on the quadrilateral (filled black circles) and the cell average denoted as a shaded circle at the center.

where $|C_{kl}|$ is the area of the cell C_{kl}. This can be easily computed in terms of vertex points (x_m, y_m) as

$$|C_{kl}| = \int_{C_{kl}} dx\,dy = \frac{1}{2}\big[(x_1 - x_3)(y_2 - y_4) - (x_2 - x_4)(y_1 - y_3)\big].$$

Following [4] the multi-moment reconstruction function in each quadrilateral can be written in terms of the local coordinates (α,β) (for convenience, dependence of the time t and indices 'kl' on the coefficients are suppressed)

$$\rho_{kl}(\alpha,\beta) = a_{00} + a_{10}\alpha + a_{01}\beta + a_{11}\alpha\beta + a_{21}\alpha^2\beta + a_{12}\alpha\beta^2 + a_{22}\alpha^2\beta^2. \tag{9}$$

On each C_{kl} the coefficients a_{ij} are uniquely determined by a set of constraints for which eight point values of $\rho(\alpha,\beta)$ from the vertices and the midpoints of the edges (see Fig. 1), as well as the cell-average value $\overline{\rho}$ are required [3,4]. The reconstruction function satisfies the conservation constraint (8). Thus for the multi-moment reconstruction process there are total nine degrees-of-freedom (dof) per each cell C_{kl}, which evolve in time. The explicit form of the coefficients in terms of nine values can be found in [3] and will not be further discussed.

3.2. SPELT algorithm on a Cartesian grid

We first consider updating the *basic* moment, the cell average $\overline{\rho}(t)$, which is responsible for preserving mass conservation. Integrating (1) spatially over the cell C_{kl} and temporally on an interval $t \in [t^n, t^{n+1}]$ results in

$$\int_{t^n}^{t^{n+1}} \int_{C_{kl}} \left(\frac{\partial \rho}{\partial t} + \nabla \cdot \mathbf{F} \right) dx\,dy\,dt = 0. \tag{10}$$

By applying the integral constraint (8) and the divergence theorem to (10) we get

$$\int_{t^n}^{t^{n+1}} \frac{\partial}{\partial t} \overline{\rho}_{kl}(t)\,dt = \frac{-1}{|C_{kl}|} \int_{t^n}^{t^{n+1}} \left(\oint_{\Gamma_{kl}} \mathbf{F} \cdot \mathbf{n}\, d\Gamma \right) dt, \tag{11}$$

where Γ_{kl} indicates the boundary of the cell C_{kl} and $\mathbf{n}$ is the unit normal vector on Γ_{kl} pointing outward with respect to the area C_{kl}. The above equation leads to the familiar finite-volume formulation

$$\overline{\rho}_{kl}^{n+1} = \overline{\rho}_{kl}^{n} - \frac{1}{|C_{kl}|} \left(\oint_{\Gamma_{kl}} \tilde{\mathbf{F}} \cdot \mathbf{n}\, d\Gamma \right), \tag{12}$$

where $\tilde{\mathbf{F}} \cdot \mathbf{n}$ may be interpreted as *exact* evolution of the fluxes on the boundaries of the cell C_{kl} along the characteristics during the time $t \in [t^n, t^{n+1}]$, as indicated in Fig. 2. Note that (12) is an exact relation for the time evolution of the spaced averaged variable $\overline{\rho}^n$ over the cell C_{kl} [18]. The accuracy and efficiency (stability) of the discretization of (12) depend on the approximation of line and time integrals [4]. Since our target is a third-order scheme, a 3-point Simpson's rule or GLL quadrature is sufficient to approximate these integrals.

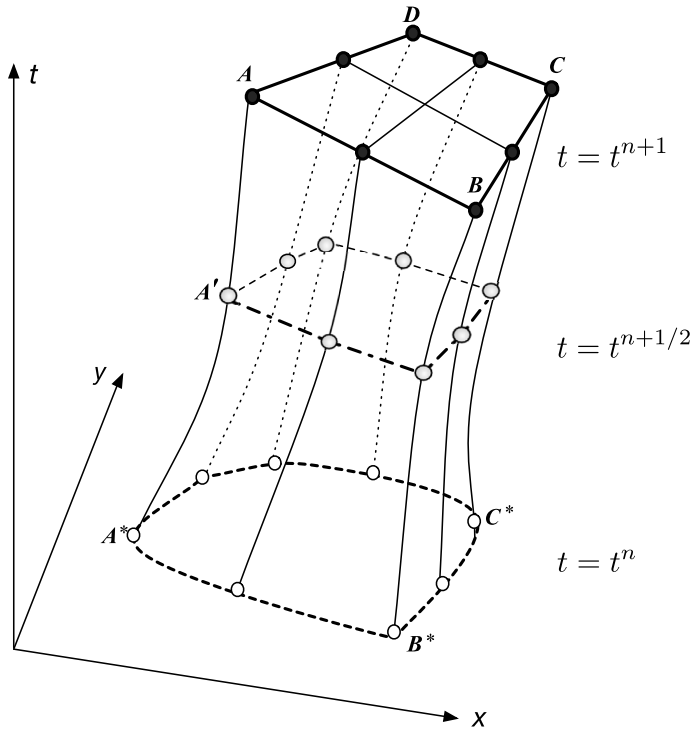

Fig. 2. Schematic diagram showing an arbitrary quadrilateral $(ABCD)$ and its upstream trajectories (or characteristics) corresponding to the corners and midpoints in (x, y, t)-space. The trajectories joining upstream points (at time $t = t^n$) and arrival points ($t = t^{n+1}$) are shown as smooth curves. The upstream points corresponding to the arrival points (filled black circles) on $ABCD$, at time level $t = t^n$ and $t = t^{n+1/2}$ are shown as open and shaded circles, respectively. Fluxes at the arrival points are computed by integrating flux values along the characteristics with respect to time.

First, we approximate the temporal integral along the characteristic. For example, the flux at point A on the quadrilateral $ABCD$ is integrated along the characteristic $A^*A'A$ as shown in Fig. 2. If we choose 3-point Simpson's rule, the time-integrated flux can be generally written as

$$\tilde{\mathbf{F}} = \int_{t^n}^{t^{n+1}} \mathbf{F}(t)\,dt \approx \frac{\Delta t}{6}\left[\mathbf{F}\left(t^n\right) + 4\mathbf{F}\left(t^{n+1/2}\right) + \mathbf{F}\left(t^{n+1}\right)\right], \tag{13}$$

where the integral requires sampling of flux values at the arrival, departure, and the midpoints (see Fig. 2). The fluxes at the departure points and midpoints are computed using (9) as the interpolating function. However, the upstream position needs to be specified in terms of local coordinates (α, β). More details are given in Appendix A.

The discretized form of (12) for the quadrilateral C_{kl} with vertices $ABCD$ as shown in Fig. 1 reads

$$\overline{\rho}_{kl}^{n+1} = \overline{\rho}_{kl}^{n} - \frac{1}{|C_{kl}|}\sum_{e=1}^{4}\int_{\Gamma_e} \tilde{\mathbf{F}}_e \cdot \mathbf{n}_e\,d\Gamma, \tag{14}$$

where Γ_e denotes a generic edge of C_{kl} with length $|\Gamma_e|$. Let $\tilde{\mathbf{F}}_e = (F_e^i, F_e^j)$ and $\mathbf{n}_e = (n_e^i, n_e^j)$ are the vector components of the flux and unit normal vectors along the (x, y) orthogonal coordinate directions. Then the line integral can be further discretized to

$$\int_{\Gamma_e} \tilde{\mathbf{F}}_e \cdot \mathbf{n}_e\,d\Gamma \approx |\Gamma_e| \sum_{\nu=1}^{3}\left[F_e^i(\nu)n_e^i + F_e^j(\nu)n_e^j\right]w_\nu, \tag{15}$$

where ν indicates the quadrature point position (flux points) with known weights w_ν, on the edge Γ_e. Thus, the cell average at new time level can be updated using (14) and (15). However, the reconstructions require eight more moments at new time level ρ_{ij}^{n+1} on the edges and corners of the cell C_{kl}. These point values at a new time level are computed via the

regular semi-Lagrangian scheme described in (3), which includes the upstream interpolation using (9):

$$\rho_{ij}^{n+1} = \left[\rho_{ij}^{n}\right]^{*}.$$

This completes the reconstruction process on each cell C_{kl}.

3.3. Monotone advection

Monotonicity or at least positivity preservation is considered to be a desirable property for transport schemes employed in many practical applications. Unfortunately, developing a monotonic limiter for high-order finite-volume scheme is not a trivial matter. We follow a practical approach based on the "flux-corrected transport (FCT)" philosophy introduced by Zalesak [35]. However, in this paper we combine FCT algorithm with SPELT only for rectangular grid systems.

An efficient way to produce non-oscillatory solution for non-conservative semi-Lagrangian transport schemes is by applying the 'quasi-monotone semi-Lagrangian' (or QMSL) filter developed in [1]. The QMSL filter has been introduced for the multi-moment transport scheme [4] for the point values ρ^{n+1}. QMSL is an *a posteriori* filter which guarantees the newly computed point values are always within the legitimate bounds such that $\rho_{\min} \leqslant \rho^{n+1} \leqslant \rho_{\max}$, where $\rho_{\min}$ and $\rho_{\max}$ are the local minimum and maximum values at previous time level in the neighborhood of the foot of the trajectory, respectively. Although this filter helps to control unphysical oscillations, the new cell averages $\overline{\rho}^{n+1}$ computed using the point values are not strictly monotonic or positivity preserving. However, we optionally apply QMSL filter for the SPELT scheme.

Essentially SPELT is a flux scheme. Therefore it is reasonable to consider a monotone algorithm such as the flux-corrected transport (FCT) introduced in [35] for limiting purpose. The FCT scheme is widely used for various flux-form transport schemes including high-order finite-volume schemes [5]. Detail reviews are available in textbooks [10,19]. Semi-Lagrangian schemes cast in conservative or flux form can also be combined with the FCT scheme to produce monotone solutions as discussed in [2,17]. The FCT scheme involves two stages, a first-order (monotone) upwind scheme is used to advect the field followed by the "antidiffusive" correction applied through a limiting process. The antidiffusive fluxes may be formally defined as

$$A_e = F_e - f_e, \tag{16}$$

where F_e is the high-order flux and f_e is the low-order (monotone) flux. The index 'e' stands for any of the four edges $(i \pm \frac{1}{2}, j)$, $(i, j \pm \frac{1}{2})$, of a rectangular cell with grid-spacing Δx and Δy. In the present context F_e is the flux computed by the SPELT scheme and f_e should be a monotone flux. The monotone flux can be computed by sweeping the flux areas as done in [17]. However, this is algorithmically complicated particularly on cubed-sphere grids. Therefore, we employ an alternative approach consistent with the SPELT algorithm. In its lowest order, the SPELT scheme using piecewise constant data degrades into the classical fully 2D donor-cell upwind method, which has the CFL restriction subject to $C_x + C_y \leqslant 1$ [6,22]. Here C_x and C_y are directional Courant numbers along the x- and y-directions, respectively. A fully 2D monotonic scheme with more relaxed CFL restriction, $\max\{C_x, C_y\} \leqslant 1$, is the corner transport upwind (CTU) method introduced by Colella [6], which we do not consider due to computational cost. In order to reduce the computational overhead associated with the monotone flux computation, we prefer the donor-cell approach with two successive time steps of length $\Delta t/2$ in the SPELT time interval $[t^n, t^{n+1}]$ (see Fig. 2). This strategy relaxes the CFL restriction associated with fully 2D donor-cell method. Furthermore, it is also computationally economical since the piecewise constant data are already available at time levels t^{n+1} and $t^{n+1/2}$ from the basic high-order SPELT scheme. Then, the resulting first-order monotone scheme corresponding to (12) can be written as

$$\rho_l^{n+1} = \rho^n - \frac{\Delta t}{2\Delta x \Delta y} \sum_{e=1}^{4} s_e \left(f_e^n + f_e^{n+1/2}\right), \tag{17}$$

where ρ_l^{n+1} is the *transported–diffused* solution used in FCT [35] with the coefficients $s_1 = s_4 = -1$ at the south and west edges, $s_2 = s_3 = 1$ at the east and north edges, respectively, of the cell with area $\Delta x \Delta y$. The flux-corrected (monotonic) high-order solution ρ_h^{n+1} is then computed as

$$\rho_h^{n+1} = \rho_l^{n+1} - \frac{1}{\Delta x \Delta y} \sum_{e=1}^{4} s_e C_e A_e, \tag{18}$$

where C_e is the correction coefficients associated with antidiffusive flux such that $0 \leqslant C_e \leqslant 1$. We follow the same procedure described in [35] to compute the coefficients C_e, and skip the details herein. Note that the computation of C_e requires the local minimum ($\rho_{\min}$) and maximum ($\rho_{\max}$) of the high-order solution at upstream cells surrounding foot of the trajectories so that $\rho_{\min} \leqslant \rho_h^{n+1} \leqslant \rho_{\max}$ [2]. A simple procedure for a positivity preserving filter, which is a special case of FCT algorithm, is described by Durran [10] and we optionally use this filter too.

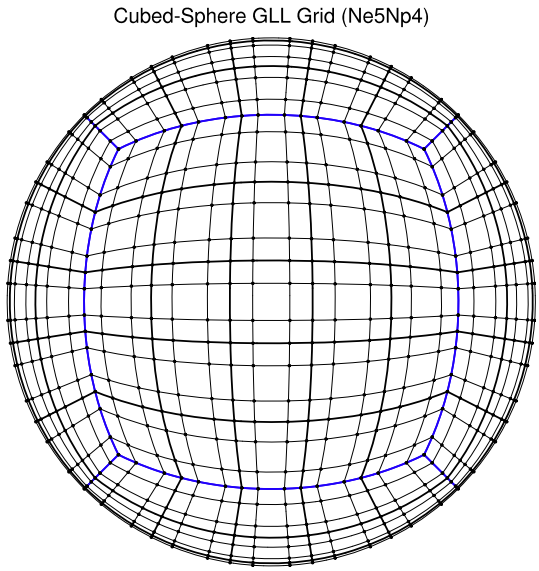

Fig. 3. A cubed-sphere grid with $6 \times N_e \times N_e$ elements where $N_e = 5$, each element has 4×4 ($N_p = 4$) GLL quadrature points shown as black dots.

3.4. SPELT on a cubed-sphere grid

The cubed-sphere geometry was originally proposed by Sadourny [30] and is used for many finite-volume and high-order Galerkin models [32,26,28,3,16,36]. Because of its nice features such as the quasi-uniform rectangular grid, cubed-sphere grid system has been adopted by many modern highly scalable dynamical cores, including the spectral-element based HOMME [31], see also Section 4. For a cubed sphere, a sphere with radius R is decomposed into six regions (sub-domains) with identical geometric properties by an equiangular central (gnomonic) projection of the faces of an inscribed cube [29, 26]. The central angles of projection $x = x(\lambda, \theta)$, $y = y(\lambda, \theta)$ are the local coordinates for each of the six faces such that $x, y \in [-\pi/4, \pi/4]$, where λ and θ are the regular longitude and the latitude, respectively. This results in a non-orthogonal curvilinear coordinate system (x, y). Fig. 3 shows a cubed sphere with $N_e \times N_e$ elements on each face. The metric tensor associated with the central projection is given by

$$g_{\imath\jmath} = \frac{R^2}{r^4 \cos^2 x \cos^2 y} \times \begin{bmatrix} 1 + \tan^2 x & -\tan x \tan y \\ -\tan x \tan y & 1 + \tan^2 y \end{bmatrix}, \tag{19}$$

with $r^2 = 1 + \tan^2 x + \tan^2 y$ and the tensor indices $\imath, \jmath \in \{1, 2\}$. The Jacobian of the transformation or the metric term is $\sqrt{g} = \sqrt{|g_{\imath\jmath}|}$, which is a smooth function and is identical in all six sub-domains with an explicit analytic form [26]. The horizontal velocity vector on the sphere $\mathbf{v}(\lambda, \theta) = (u, v)$ can be expressed in terms of contravariant (u^1, u^2) vectors on each face of the cubed sphere by

$$\begin{bmatrix} u^1 \\ u^2 \end{bmatrix} = \mathbf{A}^{-1} \begin{bmatrix} u \\ v \end{bmatrix}, \quad \mathbf{A} = R \begin{bmatrix} \cos\theta(\partial\lambda/\partial x) & \cos\theta(\partial\lambda/\partial y) \\ \partial\theta/\partial x & \partial\theta/\partial y \end{bmatrix}. \tag{20}$$

The matrix $\mathbf{A}$ is local to each face of the cubed sphere such that $G_{\imath\jmath} = \mathbf{A}^{\mathbf{T}}\mathbf{A}$. For details of the local transformation laws and the matrix $\mathbf{A}$ we refer to [26].

Although the local coordinates on each cubed-sphere face is specified in curvilinear form with (x, y) as the contravariant independent variables, the transport equation (1) can be solved on a logical cube where the local coordinates $(x, y) \in [-\pi/4, \pi/4]$ behave as in the case of a 2D Cartesian plane [26]:

$$\frac{\partial \psi}{\partial t} + \frac{\partial F_1}{\partial x} + \frac{\partial F_2}{\partial y} = 0, \quad t \in (0, T], \tag{21}$$

where $\psi = \sqrt{g}\rho$, and the fluxes are defined as $F_1 = u^1\psi$ and $F_2 = u^2\psi$ along the x- and y-directions, respectively.

The semi-Lagrangian equivalent of the advection Eq. (3) corresponding to (21) is

$$\frac{D\psi}{Dt} = 0, \quad \Rightarrow \quad \psi^{n+1} = \left[\psi^n\right]^*. \tag{22}$$

Note that in (22), ψ is the product of the metric term $\sqrt{g}$ and the true scalar ρ. The upstream interpolation $[\psi^n]^*$ is performed for the scalar ψ^n. Since the upstream value of the metric term $\sqrt{g^*}$ is known, a consistent way to recover ψ at a new time level (on the arrival grid) is as follows:

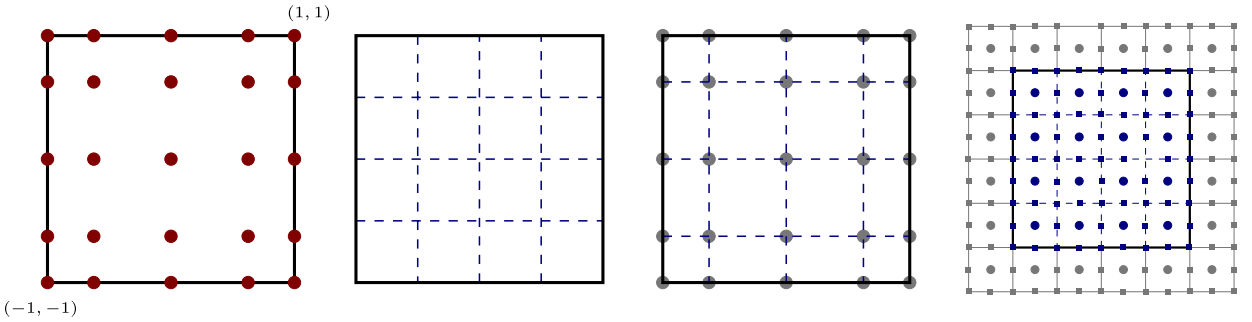

(a) Spectral element with 5×5 GLL points.

(b) Finite-volume grid with 4×4 cells.

(c) Grid based on 5×5 GLL points lead to 4×4 cells.

(d) Finite-volume grid with halo zone and unknowns.

Fig. 4. In (a) we see one spectral element with 5×5 GLL points. There exist two grids for semi-Lagrangian schemes in HOMME: in (b) we see an equi-distant cell grid and in (c) the GLL grid, which uses the GLL points to get certain cells. Subfigure (d) shows one element (bold square) and its cells and cells in the halo zone (gray cells) for a possible CFL $\leqslant 1$. The filled squares and circles represent the points for the reconstruction. Note that the reconstruction is globally continuous, so only the gray squares and circles data have to be communicated for parallelization.

$$\psi^{n+1} = \frac{\sqrt{g}}{\sqrt{g^*}} \left[\psi^n\right]^*. \tag{23}$$

4. Implementation of finite-volume schemes in HOMME

The domain decomposition (horizontal) in HOMME follows along the cubed-sphere grid. In particular, the parallel strategy relies on the spectral elements, e.g., all cube faces are divided in equi-distant meshes. A standard configuration is based on 4×4 or 5×5 Gaussian–Legendre–Lobatto (GLL) points. That means the number of unknowns for each core is at least 16 or 25 if we run the model with a minimum of one spectral element per core, e.g., Fig. 4(a) shows one spectral element with 5×5 GLL points. In [11] the CSLAM algorithm in HOMME is described in detail with its novelty of having only one communication per time step for both, using the scheme with and without monotonicity preserving filtering (both with the same amount of communication data). This approach is truly highly scalable and shows also multi-tracer efficiency. The scheme in HOMME uses an equi-distant mesh (cells) on a spectral element, see Fig. 4(b). However, the reconstruction of CSLAM, especially on the cube corner, is rather complicated and requires a deep halo zone (4 cells) including an overlap search in the halo zone. Therefore, the CFL is restricted to $\leqslant 1$ to ensure communication between neighboring spectral elements. For high-resolution meshes the original scheme becomes unstable [12]. Instead of the analytical line integral approach a Gaussian quadrature need to be applied. In order to preserve conservation of mass a consistency constraint has been enforced [12], which leads to a slightly less efficient scheme. Additionally, the search process involved in the CSLAM algorithm is computationally intense and challenging for complex domains.

The SPELT algorithm in HOMME is implemented for two different grids each based on a spectral-element discretization: the finite-volume grid and the GLL grid are shown in Fig. 4(b) and Fig. 4(c), respectively. The GLL grid leads to a highly non-uniform grid on the sphere. We emphasize that for the SPELT scheme with CFL $\leqslant 1$, it requires a halo zone of depth one (1 cell), as shown in Fig. 4(d). Furthermore, only one communication per time step (array of multiple tracers) is needed. A complicated interpolation is not needed at the cube corners as done in the CSLAM case. This is due to the compact reconstruction stencil. Note that for SPELT in HOMME we only need to find some points which belong to the Eulerian cell corresponding to the departure cell. This information can be reused for all tracers. This search is easy to implement on the cubed sphere if we have the departure point in lat/lon coordinates. In addition, we provide a positivity option with two communications per time step.

Remark 1. The positivity filter or any other filter requires information from a cell patch. It is possible reduce the communication in HOMME for the SPELT algorithm to one also when positivity filtering is applied. However, this would lead to a deeper halo zone (and therefore more values for communication) which contradicts the philosophy of designing a scheme for non-uniform or unstructured grids.

5. Numerical experiments

We first discuss the numerical results with the SPELT scheme on a non-uniform cubed-sphere grid and compare them against a uniform resolution equiangular cubed-sphere grid. Monotone results with FCT will be discussed only for the uniform resolution grid. Parallel performance of SPELT is tested in the HOMME framework.

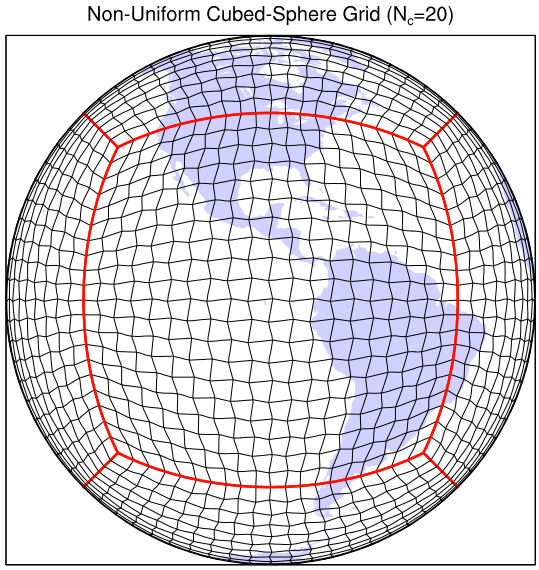

Fig. 5. Non-uniform grid on the cubed sphere with $N_c \times N_c$ finite-volume cells on each face ($N_c = 20$). The grid is generated by perturbing an equiangular uniform grid on each face so that the cells are arbitrary convex quadrilaterals. Moreover, the shape of any cell is not identical with its immediate neighbors.

5.1. Solid-body rotation tests

This is a widely used benchmark test for linear transport problems, the details of the solid-body rotation experiment are given in Williamson et al. [33]. The non-divergent spherical velocity components are defined by

$$u = u_0\big(\cos\alpha' \cos\theta + \sin\alpha' \cos\lambda \sin\theta\big), \tag{24}$$

$$v = -u_0 \sin\alpha' \sin\lambda, \tag{25}$$

where α' is the angle between the axis of the solid-body rotation and the polar axis of the spherical coordinate system. Here $u_0 = 2\pi R/12$ days such that for a complete rotation it takes 12 days of model integration [33]. If the parameter $\alpha' = 0$, the axis of rotation is the polar axis, for $\alpha' = \pi/4$, the flow field is along the north–east direction. We consider the latter case as it is more challenging on the cubed sphere since the flow follows over a cube corner. The initial scalar distribution is the cosine bell, which is a C^1 scalar field, defined as follows:

$$\rho(\lambda,\theta) = \begin{cases} \frac{\rho_0}{2}[1 + \cos(\frac{\pi r_c}{r_d})] & \text{if } r_c < r_d, \\ 0 & \text{if } r_c \geqslant r_d, \end{cases} \tag{26}$$

where $r_c = \cos^{-1}[\sin\theta_c \sin\theta + \cos\theta_c \cos\theta \cos(\lambda - \lambda_c)]$ is the great-circle distance between (λ,θ) and the bell center, initially taken as $(\lambda_c,\theta_c) = (3\pi/2, 0)$, initial bell radius $r_d = R/3$ and the *height* $\rho_0 = 1000$ units. The exact solution has the same geometry as the initial condition and is available any time of the model integration.

In addition to the cosine-bell test, we consider two more special cases for $\rho(\lambda,\theta)$ while keeping the wind field the same. They are, a smooth Gaussian profile (C^∞) for convergence tests, and a non-smooth slotted cylinder (C^0) for monotonicity tests. Smooth 2D Gaussian surfaces can be defined on a sphere using the following relation [24]:

$$\rho(\lambda,\theta) = \rho_0 \exp\big\{-h_0\big[(X - X_c)^2 + (Y - Y_c)^2 + (Z - Z_c)^2\big]\big\}, \tag{27}$$

where $\rho_0 = 1000$ units is the *height* of the Gaussian hill and parameter $h_0 = 20$ defines the base *width*. Here, (X, Y, Z) are the 3D absolute Cartesian coordinates corresponding to the spherical (λ,θ) coordinates and are related through

$$(X, Y, Z) = (R\cos\theta\cos\lambda,\ R\cos\theta\sin\lambda,\ R\sin\theta)$$

for a sphere with radius R. The center of the Gaussian distribution (X_c, Y_c, Z_c) can be specified in terms of $(\lambda_c,\theta_c) = (3\pi/2, 0)$, using the above relation. Accuracy is measured as normalized relative errors in the L^1, L^2 and L^∞ norms [33].

The *slotted-cylinder* transport problem on the Cartesian plane introduced by Zalesak [35] provides an excellent test case for monotonicity preservation and can easily be adopted for spherical geometry applications [24,17]. For non-smooth advection test we consider a slotted cylinder as the initial scalar field, which is defined by

$$\rho(\lambda,\theta) = \begin{cases} 1 & \text{if } r_c \leqslant r_d \text{ and } |\lambda - \lambda_c| \geqslant r_d/6, \\ 1 & \text{if } r_c \leqslant r_d \text{ and } |\lambda - \lambda_c| < r_d/6 \text{ and } \theta - \theta_c < -\frac{5}{12} r_d, \end{cases} \tag{28}$$

where $r_d = 1/3$, other parameters are as defined in the cosine-bell test case.

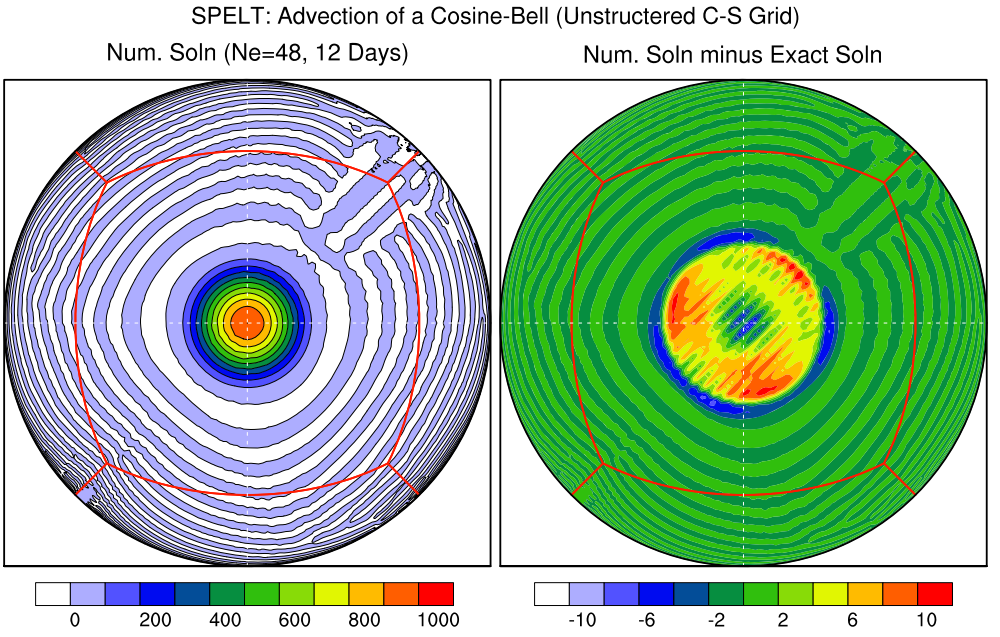

Fig. 6. An orthographic projection of numerical results on the perturbed cubed-sphere grid with $48 \times 48 \times 6$ cells. The left panel shows the cosine bell (with initial maximum 1000) after one revolution (12 days) along the north–east direction ($\alpha' = \pi/4$). The right panel shows the absolute error, a time step $\Delta t = 3600$ s is used for the simulation.

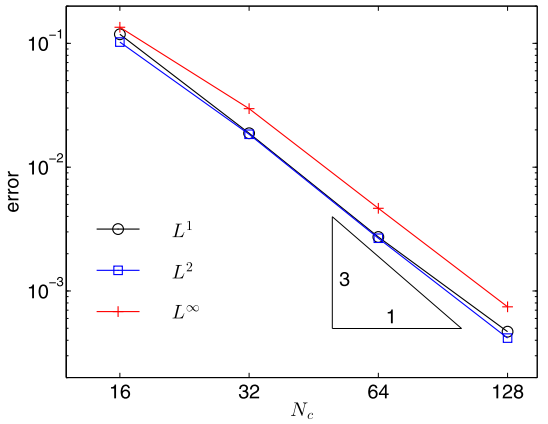

Fig. 7. Convergence of normalized errors for SPELT scheme on non-uniform grid (as shown in Fig. 5) with the Gaussian hill advection. The results are sampled after one revolution along the north–east direction, with a fixed CFL = 0.25.

5.2. SPELT transport on non-uniform cubed-sphere grids

We first consider transport with the SPELT scheme on a non-uniform grid generated by perturbing the equiangular cubed-sphere grid as shown in Fig. 5. Because of the non-uniform structure (i.e., the grid-spacing $\Delta x_{i,j} \neq \Delta x_{i+1,j}$; $\Delta y_{i,j} \neq \Delta y_{i,j+1}$), this is a challenging grid system for any high-order finite-volume scheme which requires reconstructions. However, multi-moment based approach, as used for SPELT, employs only local information within a finite-volume cell for the reconstruction process (8)–(9), and is well-suited for this type of deformed grids. The SPELT scheme requires two flux evaluations at time levels $t = t^n$ and $t = t^{n+1/2}$ as indicated in Fig. 2 along the trajectories. These flux points are located at the upstream positions corresponding to time $t - \Delta t$ and $t - \Delta t/2$, respectively, with respect to the arrival points at the time level t^{n+1}. The fluxes $\tilde{\mathbf{F}}_e$ in (15) are computed with contravariant velocity vectors, which are transformed from the given spherical (u, v) fields using (20).

Fig. 6 shows the numerical solution on the perturbed grid with $N_c = 48$ and $\Delta t = 3600$ s for a cosine-bell advection, the most widely used benchmark test for spherical advection. Even though the grid system is deformed, the solution after one revolution indicates that the SPELT scheme preserves the initial shape of the cosine bell very well. Note that no filter or limiter is used for this simulation and that the initial cell-averaged values are computed using the 9 point values with the 2D Simpson rule on each quadrilateral. As expected the maximum (absolute) error occurs at the foot of the cosine

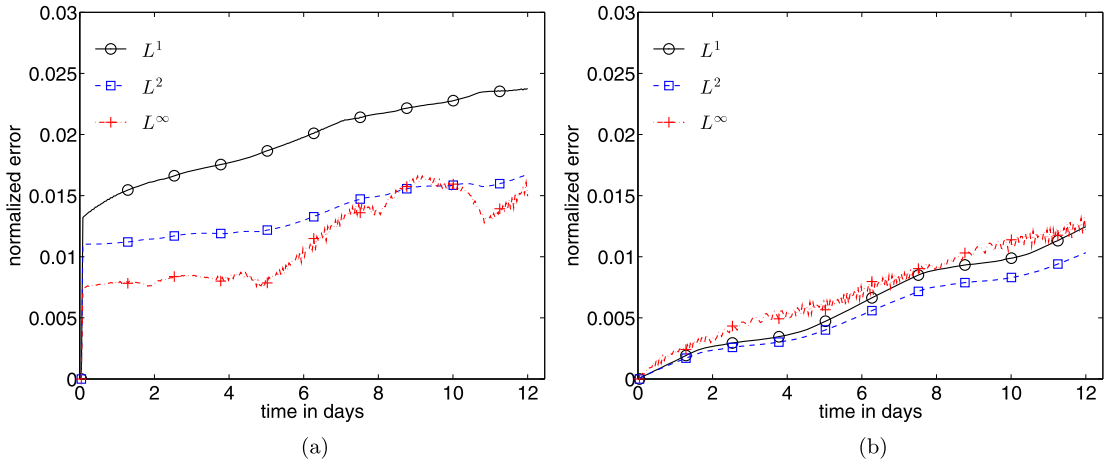

Fig. 8. Time traces of the normalized errors for the solid-body (cosine-bell) rotation problem for one complete revolution (12 days). The left panel shows errors on the perturbed grid and the right panel shows the same on the uniform grid. The resolution of the grid is $N_c = 45$ with time step $\Delta t = 1800$ s.

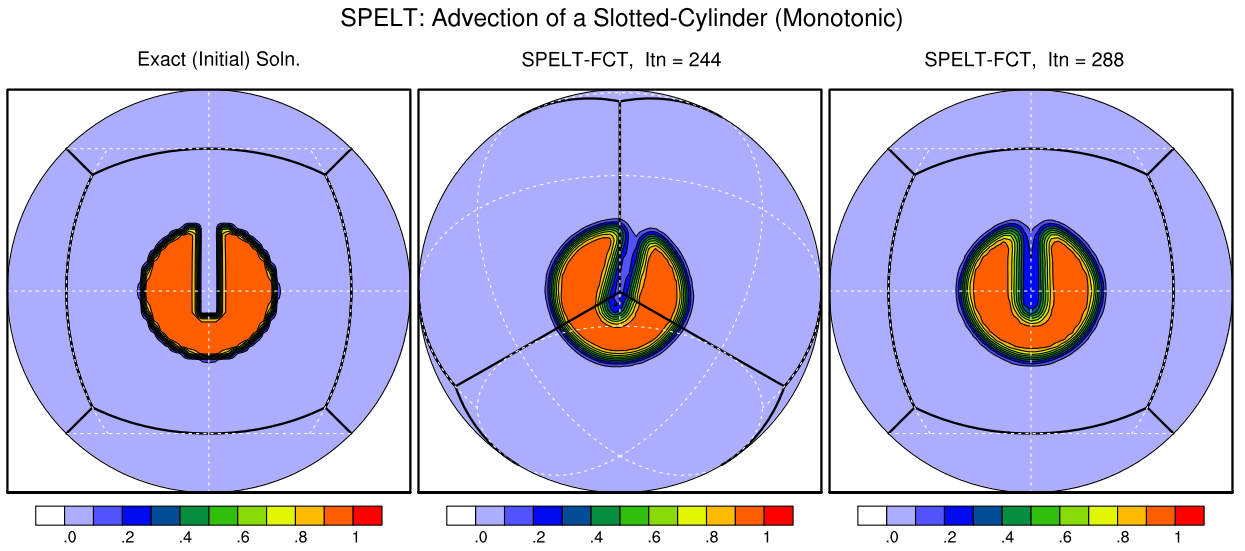

Fig. 9. Orthographic projection of the numerical solution (slotted cylinder) at different stages during complete revolution along the north–east direction. The left panel shows the initial condition and the right panel shows the final SPELT-FCT solution. The central panel shows the solution centered over a vertex of the cubed sphere at time $244\Delta t$. The uniform cubed-sphere resolution is $N_c = 48$, time step $\Delta t = 3600$ s, and the contour interval is 0.1.

bell where the solution (initial condition) is C^1 (see Fig. 6, right panel). The noise in the absolute error plot (Fig. 6, right panel) depends on the smoothness of the initial data. Experiments with Gaussian functions as initial condition show that the absolute error is much smoother. For brevity we do not show those plots. A convergence test is performed for perturbed grid (Fig. 5) using the smooth Gaussian hill initial condition (27). The convergence results are shown in Fig. 7 with a fixed CFL of 0.25. This indicates almost third-order convergence for the L^1, L^2, and L^∞ errors. Time traces of normalized errors are computed for the cosine-bell test case on both perturbed and uniform (equiangular) resolution grids as shown in Fig. 8. We do not use a filter or limiter for this test. However, SPELT on the uniform grid is more accurate than SPELT on the deformed grid.

5.3. Monotone SPELT transport on uniform cubed-sphere grids

Here we present a monotonic solution for the solid-body rotation test using the SPELT scheme combined with FCT. The initial condition $\rho(\lambda, \theta)$ is a slotted-cylinder (28) which is a non-smooth (C^0) test problem. The initial maximum height of the cylinder is 1 unit and the flow orientation is along the north–east direction. Fig. 9 shows the initial slotted cylinder (left panel) and the numerical solution at time $244\Delta t$ (centered over a corner, central panel) and $288\Delta t$ (initial position, right panel). A uniform cubed-sphere grid with $48 \times 48 \times 6$ cells used for this simulation with a time step $\Delta t = 3600$ s, so that 288 iterations are required for a complete revolution. This corresponds to a CFL = 0.625. The monotonic transport of

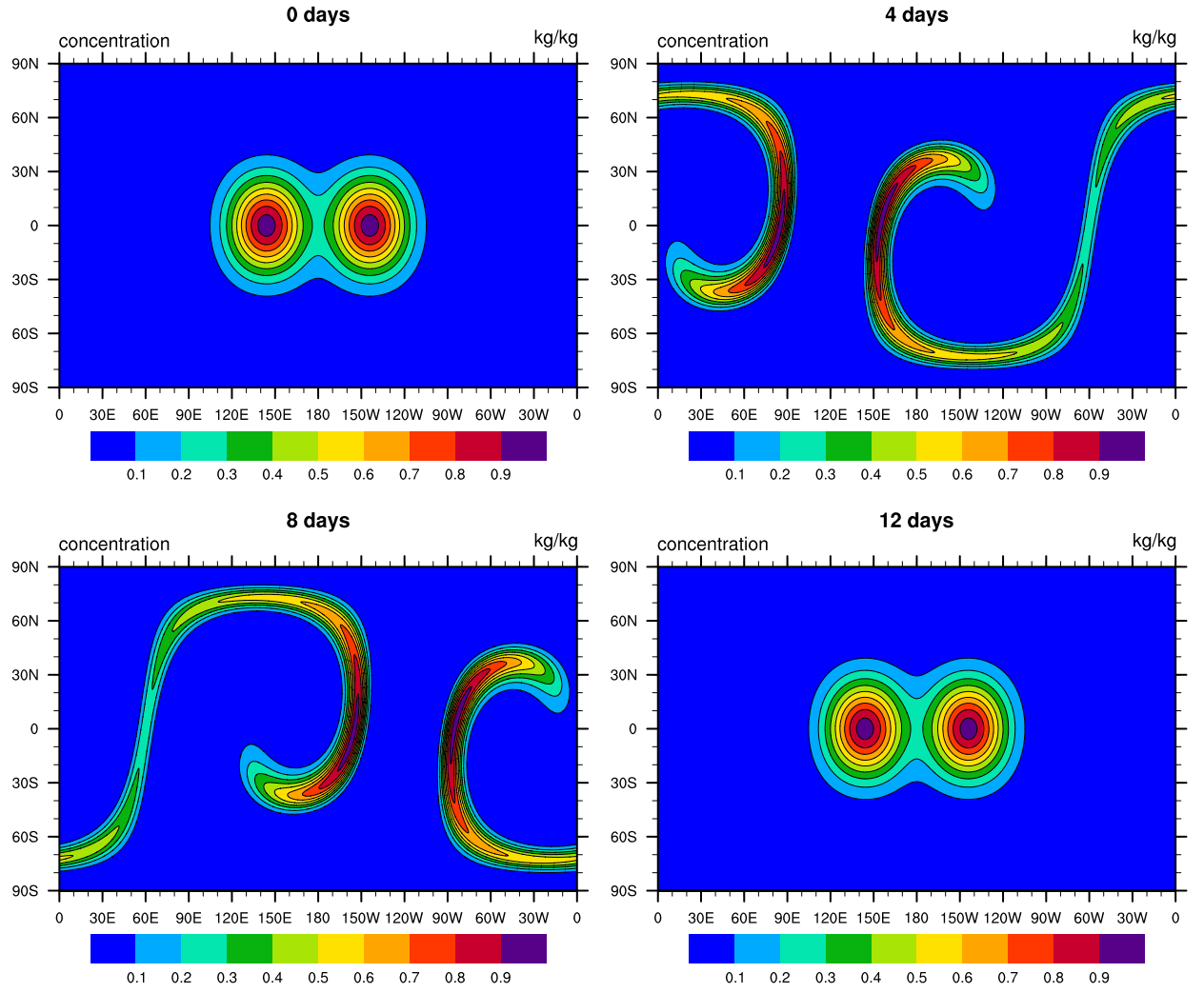

Fig. 10. Deformational test calculated with SPELT in HOMME for $N_c = 320$ and CFL $\leqslant 0.8$ with no monotonicity constraint. The Gaussian distribution returns to its initial position after 12 days.

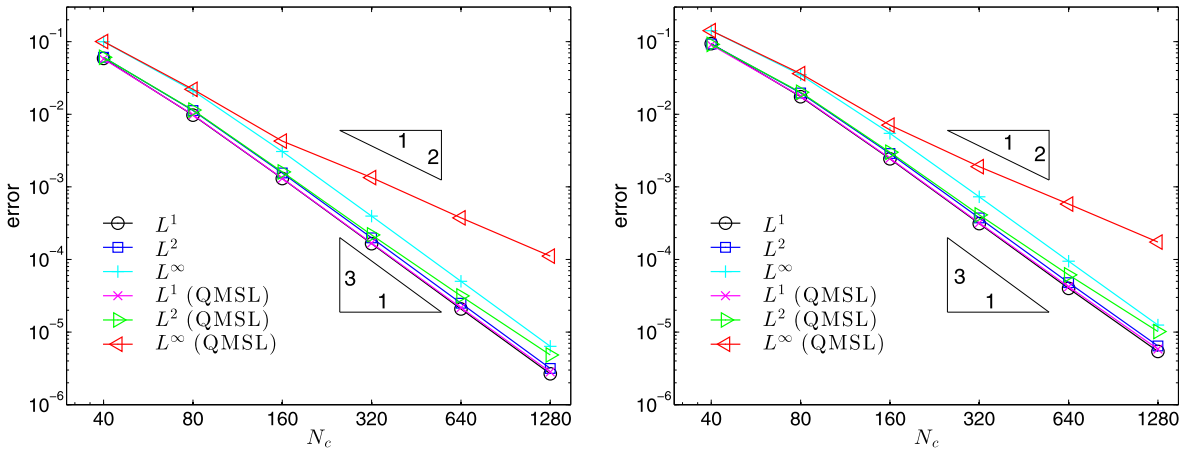

(a) Error on the finite-volume grid.

(b) Error on the GLL grid.

Fig. 11. The plots show the convergence order for different normalized error norms L^1, L^2, and L^∞ with the deformational-flow test. For this test two Gaussian hills centered at $(4\pi/5, 0)$ and $(6\pi, 5)$ (defined in Subsection 5.4) and with a CFL $\leqslant 0.8$ for (a), and CFL $\leqslant 0.87$ for (b) are used. Panels (a) and (b) show the results with the finite-volume and GLL grid, respectively, with and without QMSL filter.

the slotted cylinder is smooth across discontinuous edges and corners of the cubed sphere. The final solution appears to be slighted smoothed, however, the cylinder slot appeared to be symmetric, indicating no artifact or directional bias. The maximum height of the cylinder is 0.97 which is slightly smaller than the corresponding result reported in Harris et al. [17], but they use a CFL = 0.33.

5.4. SPELT results in the HOMME framework

We consider the smooth deformational-flow test introduced in [24] for convergence and scalability test for SPELT in HOMME. The initial distribution is similar to Gaussian hill considered for solid-body rotation case, but two Gaussian distributions are symmetrically introduced (see [24] for details). The wind field is non-divergent but highly deformational. The initial distributions are deformed into thin filaments halfway through the simulation while they are being transported along the zonal direction by the solid-body component of the flow. Note that an exact solution for this test is only available at the final time $t = T$, and it is identical to the initial condition. The time dependent non-divergent wind field is defined as

$$u(\lambda,\theta,t) = \kappa \sin^2(\lambda')\sin(2\theta)\cos(\pi t/T) + 2\pi\cos(\theta)/T,$$
$$v(\lambda,\theta,t) = \kappa \sin(2\lambda')\cos(\theta)\cos(\pi t/T),$$

where $\lambda' = \lambda - 2\pi t/T$, $\kappa = 2.0$, and $T = 5$ units. The time units can be further scaled so that 12 days are equivalent to $T = 5$, as discussed in [24]. Fig. 10 shows the time evolution of our chosen test example. For the experiments considered here we set the CFL < 1. Nevertheless, this CFL is several times higher than what would be possible for the Eulerian spectral-element advection in HOMME. We also consider a standard solid-body rotation test and the deformational-flow test with slotted cylinders (see above) in this subsection.

5.4.1. Convergence of SPELT in HOMME

To show the convergence of SPELT in HOMME all spectral elements are equi-distant on the gnomonic projection. We use either an equi-distant gnomonic grid within one spectral element as shown in Fig. 4(b) or the GLL grid as shown in Fig. 4(c) both with 4×4 cells per spectral element. We use the deformational-flow test defined above. For the finite-volume grid we choose a time step of 1600 seconds at resolution of $N_c = 40$, that means 40×40 cells for one cube face. Note that this corresponds around 2.25° at the equator and we keep the maximum CFL always $\leqslant 0.8$ (fixed) for all resolutions in our tests. For the GLL grid we have to choose a time step of 1200 seconds at a resolution of $N_c = 40$. This leads to a CFL $\leqslant 0.87$. Note that on the reference element $(-1,-1)\times(1,1)$ the GLL points for a 4×4 grid are given as $-1, -\sqrt{3/7}, 0, \sqrt{3/7}, 1$. Therefore, the smallest cell width is 0.3453. For the 4×4 finite-volume grid, however, the smallest cell width is 0.5. This explains why we have to choose a smaller time step for the GLL grid for the same number of cells on a spectral element compared to the finite-volume grid to obtain almost the same maximum CFL. Our benchmark test leads to the initial field after 12 days where we can measure the error in the L^1, L^2, and L^∞ norms. In both cases a uniform refinement simply means to divide one cell (square) in the gnomonic projection into 4 squares.

As expected, we obtain a third-order convergence rate for the deformational-flow test with infinitely smooth Gaussian surfaces and without using any filter or limiter. This is shown in Fig. 11(a)–(b). The error norms L^1, L^2, and L^∞ at day 12 are plotted for the resolutions ranging from $N_c = 40, \ldots, 1280$ for both grids. This corresponds to 2.25° to 0.07° on the equator for the finite-volume grid.[2] When we apply the QMSL filter, the convergence rate is third-order for L^1, L^2 errors and second-order for L^∞ error. We emphasize that the normalized errors for the GLL grid are higher than that for the finite-volume grid. Note that the GLL grid with the same number of cells, has a variable resolution structure due to a non-uniform distribution of quadrature points (Fig. 4(c)).

5.4.2. Error comparison of SPELT and CSLAM

In this subsection we perform a series of comparison tests with SPELT and CSLAM without using any filter or limiter. Since we also run high-resolution tests, we enforce a consistency requirement [12] for CSLAM to guarantee stability. In all cases SPELT is much more computationally efficient, see Fig. 12 and the discussion of strong scalability in Subsection 5.4.3 below. Note that the current default transport scheme in HOMME employs an explicit Runge–Kutta time stepping. The SE advection on a 4×4 GLL grid is up to fourth-order accurate. However, for smooth problems the finite-volume transport SPELT and CSLAM are third-order accurate. For the HOMME implementation, the SE advection is coupled with a hyper-diffusion operator based on an optimization algorithm [15], the resulting scheme is quasi-monotonic and its spatial accuracy is ranging from second- to fourth-order, depending on the optimization algorithm. Unfortunately, SE transport in HOMME is prohibitively expensive in the multi-tracer context. Results with SE advection in HOMME are given [15].

Table 1 shows the standard benchmark test [33] for the solid-body advection of a cosine hill defined in Subsection 5.1 of the algorithm in HOMME. The initial center is located at $(3\pi/2, 0)$, $\rho_0 = 1000$ and $r_d = (7\pi/64)R$. We show the normalized errors L^1, L^2, and L^∞ as well as the maximum and minimum of ρ for solid-body rotation test after 12 days with $\alpha' = \pi/4$. The test is performed for a resolution $N_c = 32, 64$ and $\Delta t = 4050, 2025$ s respectively. Note that SPELT is significantly more accurate than CSLAM for this test case, compare also the numbers in [4,20].

[2] The highest resolution for CAM-SE is up to 0.125°, which is considered as a very high resolution for climate simulation.

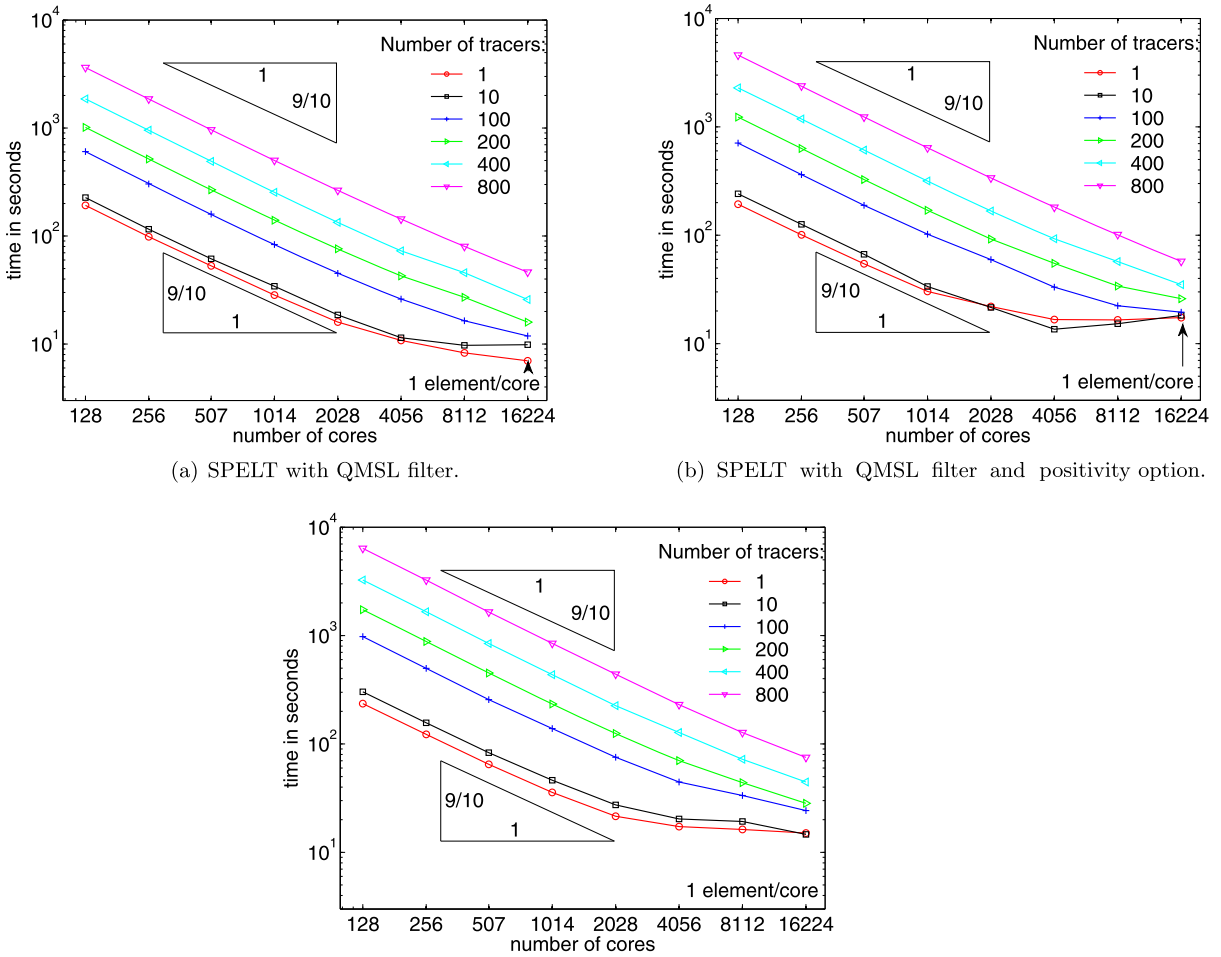

(a) SPELT with QMSL filter.

(b) SPELT with QMSL filter and positivity option.

(c) CSLAM with monotonic option.

Fig. 12. All figures show strong scalability for different numbers of tracers on Yellowstone (core-i7 Sandy Bridge). The test example is the deformational-flow test defined in Subsection 5.4 with $N_c = 208$ (2704 spectral elements per cube face) and a time step of 600 s. Note that the right most marker on each line is for 16224 cores, which corresponds to the minimum of one spectral element per core or 16 unknowns per tracer and core. Panel (a) shows the results for SPELT combined with a QMSL filter, whereas the panel (b) shows the same but with an additional positivity filter, which results in two communications per time step in our implementation. Panel (c) shows CSLAM scalability with the monotonicity option turned on.

Table 1
The normalized errors L^1, L^2, and L^∞, and the maximum and minimum of ρ are given for SPELT and CSLAM after 12 days using the standard benchmark test [33] for the solid-body advection ($\alpha' = \pi/4$). For this test the cosine hill defined in Subsection 5.1 is used. The initial center is at $(3\pi/2, 0)$, $\rho_0 = 1000$ and $r_d = (7\pi/64)R$. The results for $N_c = 32$, $\Delta t = 4050$ s and $N_c = 64$, $\Delta t = 2025$ s, respectively, are given for both schemes without any filter or limiter.

N_c	Scheme	L^1	L^2	L^∞	$\rho_{\max}$	$\rho_{\min}$
32	SPELT	4.608e−02	2.810e−02	1.661e−02	959.3	−7.67
	CSLAM	7.509e−02	4.097e−002	2.499e−02	958.9	−13.11
64	SPELT	8.502e−03	6.164e−03	4.475e−03	991.6	−3.24
	CSLAM	1.215e−02	8.164e−03	6.356e−03	991.7	−4.67

In Table 2 we show the results for the deformational-flow test with two Gaussian hills centered at $(4\pi/5, 0)$ and $(6\pi, 5)$, as defined in Subsection 5.4. For this case the resolution is such that the CFL $\leqslant 0.8$. That means, for $N_c = 40$ we choose a time step $\Delta t = 1600$ s. Note that this field is infinitely smooth and therefore we find the convergence order of 3 for both schemes in the error norms L^1, L^2, and L^∞. We also show maximum $\rho_{\max}$ and minimum $\rho_{\min}$. CSLAM has a slightly higher convergence rate (above 3) which may be a result of accurate computation of upstream integrals for infinitely smooth field.

The numbers shown in Table 3 are computed with the deformational-flow defined in Subsection 5.4 (same configuration as above), but now with two slotted cylinders centered at $(4\pi/5, 0)$ and $(6\pi, 5)$. The values are in the range $[0, 1]$. This test case is considered to be the most challenging benchmark test [24]. We observe that SPELT behaves slightly better than CSLAM in all error norms L^1, L^2, and L^∞ and in the maximum $\rho_{\max}$ and minimum $\rho_{\min}$ after 12 days.

Table 2
A comparison of the normalized errors for the smooth deformational-flow test with two Gaussian hills, located at $(4\pi/5, 0)$ and $(6\pi, 5)$, as defined in Subsection 5.4. For both schemes the CFL is always $\leqslant 0.8$, and no filter or limiter is used.

N_c	Scheme	L^1	L^2	L^∞	$\rho_{\max}$	$\rho_{\min}$
40	SPELT	5.885e−02	6.096e−02	9.965e−02	0.896	−1.451e−02
	CSLAM	8.127e−02	7.901e−02	1.215e−01	0.887	−3.000e−02
80	SPELT	9.725e−03	1.124e−02	2.109e−02	0.940	−2.226e−04
	CSLAM	8.848e−03	1.083e−02	2.079e−02	0.941	−2.869e−05
160	SPELT	1.300e−03	1.554e−03	3.068e−03	0.949	2.622e−08
	CSLAM	8.342e−04	1.070e−03	2.194e−03	0.949	2.635e−08
320	SPELT	1.649e−04	1.982e−04	3.958e−04	0.950	2.641e−08
	CSLAM	9.345e−05	1.190e−04	2.427e−04	0.950	2.642e−08
640	SPELT	2.080e−05	2.494e−05	5.008e−05	0.950	2.643e−08
	CSLAM	1.134e−05	1.440e−05	2.933e−05	0.950	2.644e−08
1280	SPELT	2.661e−06	3.152e−06	6.364e−06	0.950	2.644e−08
	CSLAM	1.424e−06	1.792e−06	3.674e−06	0.950	2.644e−08

Table 3
A comparison of the normalized errors for the non-smooth deformational-flow test as defined in Subsection 5.4 with two slotted cylinders, located at $(4\pi/5, 0)$ and $(6\pi, 5)$. The height of the cylinder (ρ) ranges in $[0, 1]$. The error norms L^1, L^2, and L^∞ and in the maximum $\rho_{\max}$ and minimum $\rho_{\min}$ are computed after 12 days. For both schemes the CFL is always $\leqslant 0.8$, and no filter or limiter is used.

N_c	Scheme	L^1	L^2	L^∞	$\rho_{\max}$	$\rho_{\min}$
40	SPELT	0.478	0.358	0.729	1.134	−0.066
	CSLAM	0.559	0.424	0.914	1.165	−0.105
80	SPELT	0.299	0.268	0.763	1.118	−0.113
	CSLAM	0.338	0.308	0.984	1.151	−0.120
160	SPELT	0.187	0.208	0.725	1.130	−0.106
	CSLAM	0.205	0.232	0.923	1.163	−0.132
320	SPELT	0.116	0.162	0.732	1.122	−0.110
	CSLAM	0.124	0.178	0.933	1.143	−0.133
640	SPELT	0.0705	0.125	0.738	1.103	−0.110
	CSLAM	0.0728	0.135	0.940	1.118	−0.131
1280	SPELT	0.042	0.096	0.730	1.104	−0.108
	CSLAM	0.042	0.103	0.929	1.116	−0.124

5.4.3. *Strong scalability of SPELT in HOMME*

Since our algorithm of SPELT in HOMME is based on the spectral-element grid, we benefit from the excellent scalability of the horizontal decomposition. Fig. 12 shows some scalability results on Yellowstone, which is the new (2013) petascale computing resource in the NCAR-Wyoming Supercomputing Center. Yellowstone is a 1.5-petaflops high-performance computing system with 2.6-GHz Intel Sandy Bridge cores and 2 GB memory/core.[3] A standard user can allocate up to 16 384 cores. For our test we run our benchmark test using a problem size of 16 224 spectral elements (equi-distant mesh on the cubed sphere), which allows us to test our algorithm for one element per core. Each of these elements is divided in 4×4 cells (equi-distant finite-volume grid) as in Fig. 4(b). This results in 2704 spectral elements per cube face or 43 264 cells. To ensure CFL $\leqslant 1$ we allow a time step of 600 seconds. For all tests we disable I/O. Fig. 12 shows the strong scalability with respect of the number of cores. The right most marker on each line is for 16 224 cores and corresponds to one spectral element per core or 16 unknowns per core and per tracer. In Fig. 12(a) we plot the results for SPELT. The scheme scales for all tracers, however, for $1 \ldots 10$ tracers one can clearly see the latency due to an overhead in communication time. Or in other words the scheme can simply not use entirely the high number of cycles of a core. The scalability is almost ideal for 4 elements (or 64 unknowns per tracer) per core. Increasing the number of tracers (more than 100) leads to perfect scaling (0.9) also for 1 element per core. In Fig. 12(b), however, one can clearly see the effect of the second communication when positivity preserving option is applied. For 4 elements per core we still have almost perfect scaling for all tracers. The algorithm does not scale below 4 elements per core and 1–10 tracers but scales again for more than 100 tracers. We compare our results for SPELT with the scalability of CSLAM on Yellowstone shown in Fig. 12(c). We stress that the scalability of CSLAM is similar to Fig. 12(b) for a low number of tracers and element per core, which is due to the higher communication load of the scheme (CSLAM has 128 and SPELT 88 values to communicate per tracer and element, respectively). However,

[3] https://www2.cisl.ucar.edu/resources/yellowstone.

the SPELT algorithm with positivity filter (and therefore two communications per time step) is faster for more tracers or more elements per core. All runs show also the multi-tracer efficiency of SPELT.

Remark 2. The work in [11] shows scalability for the CSLAM algorithm considered here. There, scalability was also good for the configuration of one element per core. Note that the tests were done only on 4096 cores on an IBM Blue Gene/L system with a much slower CPU per core.

6. Conclusions

We have presented a new conservative semi-Lagrangian scheme (SPELT) on arbitrary quadrilateral spherical grids. SPELT is a flux-based characteristic semi-Lagrangian method where the fluxes are integrated along the trajectory. This avoids computationally expensive and cumbersome upstream overlap-area searching, as required in regular conservative semi-Lagrangian methods. Therefore, the implementation on complex grids and for super computers is relatively easy. The reconstruction procedure for SPELT employs a single-cell based multi-moment approach which results in a computationally desirable compact stencil. Moreover, it can be extended to arbitrary convex quadrilateral grids or unstructured grid systems. The SPELT scheme is formally third-order accurate and shows good convergence on highly deformed non-uniform grids. Currently, SPELT is tuned for a CFL $\leqslant 1$. However, this limit could be extended by using more accurate flux integrals at additional computational expenses. Monotonic (positivity) options for solutions on uniform resolution grids are available for the SPELT scheme when combined with the flux-corrected transport (FCT) algorithm. The monotonicity option was tested using a standard benchmark, solid-body rotation of a slotted cylinder, and the SPELT-FCT combination produces excellent quality solution with shape preservation.

HOMME (High-Order Method Modeling Environment) is a highly scalable dynamical core which relies on cubed-sphere grid system with non-uniform spectral-element tiling, and supports unstructured grids. The primary motivation for developing SPELT was to extend the HOMME framework to facilitate multi-tracer efficient semi-Lagrangian transport without impeding its parallel efficiency. SPELT was tested in HOMME framework using a benchmark deformational-flow test. Several convergence tests were performed to show the robustness and accuracy for our scheme for high-resolution meshes. Multi-tracer efficiency and scalability were demonstrated on a state-of-the-art supercomputer, and for a higher number of tracers (mimicking the real multi-tracer applications) we get excellent *strong* scalability. In terms of computational efficiency SPELT is significantly faster than CSLAM. In terms of accuracy both finite-volume schemes, SPELT and CSLAM, are comparable. However, for smooth fields CSLAM seems to be slightly more accurate than SPELT, but for non-smooth or quasi-smooth fields SPELT is slightly more accurate than CSLAM.

Since SPELT is a flux-based scheme, it is possible to combine flux limiters to control spurious oscillations on unstructured grids, which is something we plan to examine in the near future. Since HOMME is the default dynamical core of the climate model CAM-SE it is our ultimate goal to run SPELT in CAM-SE with hundreds of tracers, where the air mass comes from the spectral-element dynamical core and the passive tracer transport is done by SPELT. In a future work we will focus on the consistent coupling between air mass and tracer concentration. This will increase the performance of future climate simulation in CAM-SE, since SPELT allows a larger time step and is more efficient for more tracers than the current spectral-element tracer algorithm.

Acknowledgements

The authors gratefully acknowledge the careful internal review by Dr. Robert Klöfkorn (National Center for Atmospheric Research, USA). The authors were partially supported by the DOE BER Program under award DE-SC0006959. Parts of this work were done when both authors participated the Multiscale Numerics for the Atmosphere and Ocean program at the Isaac Newton Institute (INI) for Mathematical Sciences, Cambridge, UK. We thank Dr. Hilary Weller (University of Reading, UK) and one anonymous reviewer for their very helpful comments and suggestions that have significantly improved this manuscript.

Appendix A

Semi-Lagrangian schemes require upstream interpolation to update the values at arrival points. For the SPELT scheme, the reconstruction functions (9) are defined in terms of local (α, β) coordinates on each Eulerian cell C_{kl}, which can be used as an interpolant. The departure points are usually specified in the cubed-sphere coordinates (x, y), and the cell that containing these points can be searched. Once the departure cell is identified, the *global* coordinates (x, y) need to be transformed in terms of local (α, β) coordinates using (4) and (5), such that $\alpha, \beta \in [0, 1]$. However, the inverse mapping corresponding to the parametric representation (4) and (5) is no more linear. To start with we first use (4) to find α

$$\alpha = \frac{x - a_1 - a_3\beta}{a_2 + a_4\beta}. \tag{A.1}$$

Elimination α from (5) using (A.1) yields to the following quadratic equation:

$$A\beta^2 + B\beta + C = 0, \tag{A.2}$$

where the coefficients

$$A = a_4 b_3 - a_3 b_4,$$
$$B = a_4 b_1 - a_1 b_4 + a_2 b_3 - a_3 b_2 + x b_4 - y a_4,$$
$$C = a_2 b_1 - a_1 b_2 + x b_2 - y a_2.$$

Therefore, β can be solved directly from (A.2), $\beta = (-B + \sqrt{B^2 - 4AC})/2A$. Nevertheless, this formula may fail in some extreme cases due to precision error. In such cases a Newton–Raphson approach would be desirable to solve (A.2). Then α is recovered from (A.1).

References

[1] R. Bermejo, A. Staniforth, The conversion of the semi-Lagrangian advection schemes to quasi-monotone schemes, Mon. Weather Rev. 120 (1992) 2622–2632.
[2] P.N. Blossey, D.R. Durran, Selective monotonicity preservation in scalar advection, J. Comput. Phys. 227 (2008) 5160–5183.
[3] C. Chen, F. Xiao, Shallow water model on cubed-sphere by multi-moment finite volume method, J. Comput. Phys. 227 (2008) 5019–5044.
[4] C.G. Chen, F. Xiao, X.L. Li, Y. Yang, A multi-moment transport model on cubed-sphere grid, Int. J. Numer. Methods Fluids 56 (2010) 567–584.
[5] V. Cheruvu, R.D. Nair, H.M. Tufo, A spectral finite volume transport scheme on the cubed-sphere, Appl. Numer. Math. 57 (2007) 1021–1032.
[6] P. Colella, Multidimensional upwind method for hyperbolic conservation laws, J. Comput. Phys. 87 (1990) 171–200.
[7] J.M. Dennis, J. Edwards, K.J. Evans, O. Guba, P.H. Lauritzen, A.A. Mirin, A. St-Cyr, M.A. Taylor, P.H. Worley, CAM-SE: A scalable spectral element dynamical core for the Community Atmosphere Model, Int. J. High Perform. Comput. Appl. 26 (2012) 74–89.
[8] J.M. Dennis, A. Fournier, W.F. Spotz, A. St-Cyr, M.A. Taylor, S.J. Thomas, H.M. Tufo, High resolution mesh convergence properties and parallel efficiency of a spectral element atmospheric dynamical core, Int. J. High Perform. Comput. Appl. 19 (2005) 225–235.
[9] J.K. Dukowicz, J.R. Baumgardner, Incremental remapping as a transport/advection algorithm, J. Comput. Phys. 160 (2000) 318–335.
[10] D.R. Durran, Numerical Methods for Fluid Dynamics with Application Geophysics, second ed., Springer-Verlag, 2010.
[11] C. Erath, P.H. Lauritzen, J.H. Garcia, H.M. Tufo, Integrating a scalable and efficient semi-Lagrangian multi-tracer transport scheme in HOMME, Proc. Comput. Sci. 9 (2012) 994–1003.
[12] C. Erath, P.H. Lauritzen, H.M. Tufo, On mass-conservation in high-order high-resolution rigorous remapping schemes on the sphere, Mon. Weather Rev. 141 (6) (2013) 2128–2133.
[13] C. Erath, M. Taylor, R. Nair, Efficiency of semi-Lagrangian schemes SPELT and CSLAM compared to the Spectral Element transport scheme in CAM-SE, 2013, in preparation.
[14] F.X. Giraldo, Lagrange–Galerkin methods on spherical geodesic grids: the shallow water equations, J. Comput. Phys. 160 (2000) 336–368.
[15] O. Guba, M. Taylor, A. St-Cyr, Optimal limiters for the spectral element method, J. Comput. Phys. (2013), submitted for publication.
[16] W. Guo, R.D. Nair, J. Qui, A conservative semi-Lagrangian discontinuous Galerkin scheme on the cubed-sphere, Mon. Weather Rev. (2013), http://dx.doi.org/10.1175/MWR-D-13-00048.1, in press.
[17] L.M. Harris, P.H. Lauritzen, R. Mittal, A flux-form version of the conservative semi-Lagrangian multi-tracer transport scheme (CSLAM) on the cubed sphere grid, J. Comput. Phys. 230 (2011) 1215–1237.
[18] C. Hirsch, Numerical Computation of Internal and External Flows: Fundamentals of Computational Fluid Dynamics, Elsevier, ISBN 978-0-7506-6594-0, 2007, 656 pp.
[19] D. Kuzmin, R. Lohner, S. Turek (Eds.), Flux-Corrected Transport: Principles, Algorithms, and Applications, Scientific Computation, Springer, 2012.
[20] P.H. Lauritzen, R.D. Nair, P.A. Ulrich, A conservative semi-Lagrangian multi-tracer transport scheme (CSLAM) on the cubed-sphere grid, J. Comput. Phys. 229 (2010) 1401–1424.
[21] B.P. Leonard, A.P. Lock, M.K. MacVean, Conservative explicit unrestricted-time-step multidimensional constancy-preserving advection schemes, Mon. Weather Rev. 124 (1996) 2588–2606.
[22] R.J. LeVeque, Finite Volume Methods for Hyperbolic Problems, Cambridge University Press, ISBN 0-521-00924-3, 2002, 558 pp.
[23] S.-J. Lin, R.B. Rood, Multidimensional flux-form semi-Lagrangian transport scheme, Mon. Weather Rev. 124 (1996) 2046–2070.
[24] R.D. Nair, P.H. Lauritzen, A class of deformational flow test cases for linear transport problems on the sphere, J. Comput. Phys. 229 (23) (2010) 8868–8887.
[25] R.D. Nair, B. Machenhauer, The mass-conservative cell-integrated semi-Lagrangian advection scheme on the sphere, Mon. Weather Rev. 130 (2002) 649–667.
[26] R.D. Nair, S.J. Thomas, R.D. Loft, A discontinuous Galerkin global shallow water model, Mon. Weather Rev. 133 (2005) 876–888.
[27] M.R. Norman, R.D. Nair, F.H.M. Semazzi, A low communication and large time step explicit finite-volume solver for non-hydrostatic atmospheric dynamics, J. Comput. Phys. 230 (2011) 1567–1584.
[28] W.M. Putman, S.J. Lin, A finite-volume dynamical core on the cubed-sphere grid, in: Numerical Modeling of Space Plasma Flows: ASTRONUM-2008, in: Astronomical Society of the Pacific Conference Series, vol. 406, 2009, pp. 268–275.
[29] C. Ronchi, R. Iacono, P.S. Paolucci, The "cubed sphere": A new method for the solution of partial differential equations in spherical geometry, J. Comput. Phys. 124 (1) (1996) 93–114.
[30] R. Sadourny, Conservative finite-difference approximations of the primitive equations on quasi-uniform spherical grids, Mon. Weather Rev. 100 (1972) 136–144.
[31] M. Taylor, J. Edwards, S. Thomas, R. Nair, A mass and energy conserving spectral element atmospheric dynamical core on the cubed-sphere, J. Phys. Conf. Ser. 78 (2007).
[32] M. Taylor, J. Tribbia, M. Iskandarani, The spectral element method for the shallow water equations on the sphere, J. Comput. Phys. 130 (1997) 92–108.
[33] D. Williamson, J. Drake, J. Hack, R. Jakob, P. Swarztrauber, A standard test set for numerical approximations to the shallow water equations in spherical geometry, J. Comput. Phys. 102 (1992) 211–224.
[34] F. Xiao, R. Akoh, S. Ii, Unified formulation for compressible and incompressible flows by using multi-integrated moments II: Multi-dimensional version for compressible and incompressible flows, J. Comput. Phys. 213 (2006) 31–56.
[35] S.T. Zalesak, Fully multidimensional flux-corrected transport algorithms for fluids, J. Comput. Phys. 31 (1979) 335–362.
[36] Y. Zhang, R.D. Nair, A nonoscillatory discontinuous Galerkin transport scheme on the cubed-sphere, Mon. Weather Rev. 140 (2012) 3106–3126.